

Dynamical phase transition in models that couple chromatin folding with histone modificationsAmogh Sood , Greg Schuette , and Bin Zhang **Department of Chemistry, Massachusetts Institute of Technology, Cambridge, Massachusetts 02139, USA*

(Received 1 November 2022; revised 26 February 2024; accepted 25 April 2024; published 24 May 2024)

Genomic regions can acquire heritable epigenetic states through unique histone modifications, which lead to stable gene expression patterns without altering the underlying DNA sequence. However, the relationship between chromatin conformational dynamics and epigenetic stability is poorly understood. In this paper, we propose kinetic models to investigate the dynamic fluctuations of histone modifications and the spatial interactions between nucleosomes. Our model explicitly incorporates the influence of chemical modifications on the structural stability of chromatin and the contribution of chromatin contacts to the cooperative nature of chemical reactions. Through stochastic simulations and analytical theory, we have discovered distinct steady-state outcomes in different kinetic regimes, resembling a dynamical phase transition. Importantly, we have validated that the emergence of this transition, which occurs on biologically relevant timescales, is robust against variations in model design and parameters. Our findings suggest that the viscoelastic properties of chromatin and the timescale at which it transitions from a gel-like to a liquidlike state significantly impact dynamic processes that occur along the one-dimensional DNA sequence.

DOI: [10.1103/PhysRevE.109.054411](https://doi.org/10.1103/PhysRevE.109.054411)**I. INTRODUCTION**

Eukaryotic cells compactly package their genome into chromatin that consists primarily of nucleosomes formed by DNA wrapping around histone proteins [1,2]. These core histones are often subject to post-translational marking, including acetylation and methylation, [3,4] which partitions chromosomes into distinct domains with differential transcription activity [5–21], providing active (euchromatic) and inactive (heterochromatic) regions with characteristic chemical signals. The coexistence of stretches of chromatin enriched and depleted of specific histone marks implies multistability in epigenetic regulation [9,22].

Many theoretical models have been introduced to study the stability of histone marks [23–33]. Positive feedback underpins these models since existing marks recruit enzymes to confer similar marks at new nucleosomes [34–38]. The 3D structure of the genome births this feedback as chromatin loops bringing nucleosomes far apart in sequence into spatial proximity facilitating long-range spreading of histone marks [39–42]. Additionally, chemical modifications also affect nucleosome-nucleosome interactions, either by directly altering the physicochemical properties of amino acids or by recruiting additional protein molecules [43–48], impacting chromatin organization. Therefore, chromatin is an instructive scaffold inextricably linked to epigenetic regulation [49–51].

Explicitly accounting for chromatin organization when studying histone marks has become increasingly important in recent studies [52–61]. Early efforts in coupling chromatin structure and epigenetic reaction networks primarily relied on mean-field models, either assuming fully connected nucleosomal sites or incorporating power-law contact probabilities

between sites to allow for long-range spreading of marks [24,25,55]. Many groups expanded on these ideas by extracting nucleosome contacts with explicit polymer simulations when modeling histone modification kinetics [59–67]. Furthermore, recent work has revealed that chromatin exhibits nontrivial rheology and viscoelastic properties, with multiple, disparate relaxation timescales, and organizes into regions of varying mobility [68–76]. In particular, *in vivo* studies of chromatin report solidlike behavior [77–79] and structural relaxation occurring on the timescale of hours, comparable to the rate of enzyme-mediated histone modifications [32,80,81]. However, explicit coupling between the chromatin structure and epigenetic modifications, and a systematic interrogation of the concomitant impact of timescale separation between their dynamics, is underexplored in existing literature, necessitating further investigation. Furthermore, the nature of steady states produced by existing models requires additional deliberation. While they support the multistability of distinct histone modification patterns, the modified states often adopt identical, compact chromatin conformations [52–61]. However, numerous studies that probed chromatin organization with various techniques have revealed dramatic structural differences among chromatin with distinct modifications [82,83]. A more biologically relevant outcome would correspond to two states that support an open, unmarked (euchromatin) and collapsed, marked chromatin (heterochromatin). Models supporting structural changes between steady states would better represent biological systems and provide deeper insight into chromatin stability.

II. MODEL

We present a theoretical model with explicit coupling between chromatin conformational dynamics and histone modifications (Fig. 1). The vector $\mathbf{n}(t) \equiv \{n_i(t)\}$ for $i \in [1, N]$

*binz@mit.edu

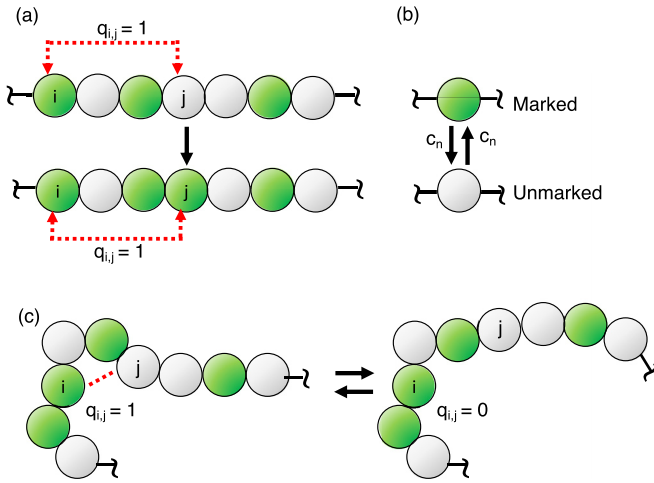
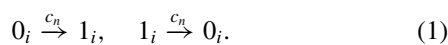


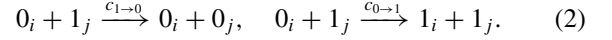
FIG. 1. A schematic illustration of the salient features of a kinetic model explicitly accounting for the interdependence between changes in histone marks and chromatin contacts. Green and grey circles indicate marked and unmarked nucleosomes, respectively. (a) Marks can be added (or removed) via an enzyme-mediated recruited process wherein two sites that are in contact become similarly modified [Eq. (2)]. $q_{ij} = 1$ indicates a direct contact in 3D space between two nucleosomes (i and j) separated in a linear sequence. (b) Nucleosomes can also be marked (or unmarked) via random conversions occurring independent of chromatin contacts [Eq. (1)]. (c) Chromatin conformational dynamics are modeled as stochastic transitions in contact space, where contact formation (breaking) rates depend on polymer topology and nucleosome marks.

of length N denotes the chemical state of chromatin at any given time, t . The binary variable, $n_i \in \{0, 1\}$, indicates the presence (or absence) of a histone mark at nucleosome i . Inspired by protein-folding literature [84–87], we adopt a contact space representation of the chromatin conformation. A vector of size \mathbf{M} , $\mathbf{q}(t) \equiv \{q_{ij}(t)\}$ for $i, j \in [1, N]$ and $j - i > 1$ represents the chromatin conformation at time t . $q_{ij} \in \{0, 1\}$ is again a binary variable denoting the presence (or absence) of 3D contacts between a pair of nucleosomes (i, j). Neighboring nucleosomes are always assumed to be in contact (i.e., $q_{i,i+1} = 1$). Similar to explicit polymer simulations, this model allows the coupling of histone chemical kinetics with instantaneous chromatin structural changes. Importantly, no assumptions about the timescale separation are needed, and rigorous stochastic simulation algorithms can be employed to examine the dynamical coupling across a wide range of timescales.

Following previous studies [24–26], two types of reactions that drive changes in histone marks are considered. First is an on-site, random conversion that arises from exchanging histone proteins with the nucleoplasm or reactions catalyzed by noncooperative enzymes. For example, an unmarked nucleosome i with $n_i = 0$ (0_i) can become marked with $n_i = 1$ (1_i) at a basal rate c_n independent of chromatin conformation and the state of other nucleosomes. Similarly, marked nucleosomes can be converted back to unmarked ones. The corresponding reaction schemes are



The second is recruited conversions, a measure of cooperativity in the system, ensuring nucleosomes in spatial proximity are similarly marked. These reactions can arise due to the transfer of enzymes among nucleosomes in contact. We consider the cooperative effect for both addition and removal enzymes. Therefore, for a pair of contacting nucleosomes (i, j) in different chemical states, either the mark at site j is removed or a new mark is introduced to site i via recruited conversions as denoted below:



Both reactions occur with rate c_r unless otherwise specified.

We treat chromatin conformational dynamics analogously as stochastic transitions in contact space. The rates of contact formation and dissolution are influenced by the interplay between the attraction among modified nucleosomes and the entropic effects stemming from homopolymer dynamics. However, due to the lack of precise expressions for polymer entropy within contact space and, consequently, for these rates, we investigate three different approximations of increasing simplicity.

First, in Sec. II A, we devise an Ising-like Hamiltonian to replicate contact statistics obtained from molecular dynamics simulations of a homopolymer model [88–91]. This Hamiltonian provides a microscopic framework for describing the stochastic transition of individual contacts, incorporating both the entropic costs associated with contact formation and the pairwise correlation between contacts. Using this schema, we observe, that in transitioning from a slow to a fast chromatin regime, the system undergoes a dynamic phase transition, marked by three key signatures. First, the system’s steady-state probability distribution for a fraction of contacts made shifts from being monostable to bistable. Simultaneously, the probability distribution for a fraction of nucleosomal sites marked becomes skewed and asymmetric. Lastly, there is a concomitant divergence in the average lifetimes of marked and unmarked states. Subsequently, in Sec. II B, we introduce a mean-field expression for polymer entropy to examine the impact of specific parameters of the Ising Hamiltonian on our findings. Our analysis confirms that the mean-field model qualitatively reproduces the key results outlined in Sec. II A. Finally, in Sec. II C, we propose a phenomenological master equation that does not rely on explicit expressions for polymer entropy. Here, we treat contact formation (and disruption) akin to a birth-death process and consider the marks as a two-level system, while explicitly addressing the interconnected dynamics of chromatin contacts and histone modifications. These simplifications make the model partially analytically tractable. Using this phenomenological model, we show that the observed dynamical phase transition in the preceding models emerges from the coupling of structure and sequences, rather than from specific treatments of free energy functionals in contact space. Additionally, we estimate that the average lifetime near the critical birth rate of contacts aligns approximately with predictions in contemporary literature [76,77,92].

A. An Ising-like Hamiltonian for chromatin contacts

To describe the microscopic dynamics of chromatin conformation in contact space, we introduce the following

Hamiltonian, $\mathcal{H}(\mathbf{q})$, defined as:

$$\begin{aligned} \mathcal{H}(\mathbf{q}) = & \sum_{j>i} h_{ij} q_{ij} + \sum_{j>i} \sum_{l>k} J_{ijkl} q_{ij} q_{kl} \\ & + \lambda \sum_{j>i} q_{ij} \sum_{k \neq i,j} (q_{ik} + q_{kj}). \end{aligned} \quad (3)$$

The linear term, h_{ij} , accounts for the entropic penalty of bringing nucleosomes i and j into contact [88]. The symmetric term $J_{ijkl} = J_{klij}$ accounts for the coupling of contact formation between distinct pairs of nucleosomes [91]. This coupling emerges whenever the existence of contact (i, j) affects the configurational entropy penalty associated with forming contact (k, l) as a result of polymer topological effects [89,90]. We follow a preexisting pseudolikelihood maximization approach [93] to obtain all parameters, h_{ij} and J_{ijkl} , that most likely to reproduce the statistical distribution of a set of homopolymer configurations that resemble *in vivo* chromatin organization. We refer readers to Appendix A for details. The λ term in Eq. (3) accounts for the excluded volume effect by penalizing the formation of multiple contacts with the same nucleosome. Similar models have been applied successfully to study protein folding mechanisms [86,87].

From the above Hamiltonian, we define the rate of breaking and forming a contact between nucleosomes i and j as $k_c \exp(-\beta \epsilon n_i n_j \Delta q_{ij})$ and $k_c \exp(-\beta \Delta \mathcal{H})$, respectively. These terms account for the energetic and entropic costs of contact breaking and formation, assuming contact formation is diffusion limited [94,95]. Here k_c is the basal rate constant and is representative of thermal nucleosomal motions. $\beta = 1/k_B T$ and k_B is the Boltzmann constant. $\epsilon = -2.5 k_B T$ measures the interaction energy between marked nucleosomes. This attraction is meant to account for the effects of architectural proteins associated with epigenomic states that aid 3D chromatin organization [96]. The order of magnitude of this parameter was chosen to be comparable to values estimated from force spectrometry experiments [97]. $\Delta \mathcal{H} = \mathcal{H}(\mathbf{q}|q_{ij} = 1) - \mathcal{H}(\mathbf{q}|q_{ij} = 0)$.

Without explicit chromatin conformational dynamics and $q_{ij} = 1 \forall i, j \in [1, \mathbf{N}] \forall t$, the above model reduces to an extensively studied mark-only version [25,26,28,57,59] which exhibits bistability with two steady states where the fraction of marked nucleosomes is either close to 1 or to 0 for large c_r values. Hereon, the values for all rate constants are reported in the unit of c_n . We focus on a strongly cooperative regime wherein $c_r = 100$.

Following contemporary literature, we first explore the regime where chromatin conformational dynamics are fast and choose $k_c = 10^3$. We interrogate the system using stochastic simulations performed with the Gillespie algorithm [98]. Since c_n has been estimated to be around 0.6 h^{-1} [99], this value for k_c corresponds to nucleosome motions on the second timescale, which matches well with experimental estimations from live cell imaging [92]. Figure 2(a) shows an example trajectory initialized with zero chromatin contacts and marked nucleosomes. The blue and red traces depict the time evolution of the fraction of marked nucleosomes ($\bar{n} \equiv \sum_i n_i / \mathbf{N}$) and the fraction of contacts formed ($\bar{q} \equiv \sum_{ij} q_{ij} / \mathbf{M}$), respectively. Initially, transitions to the fully marked state are unsuccessful without sufficient

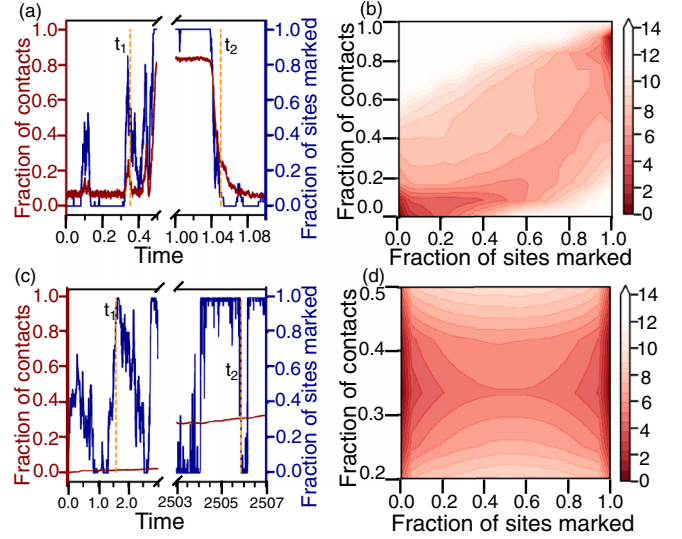


FIG. 2. The model exhibits distinct kinetic and steady-state behaviors in fast and slow chromatin dynamics regimes. (a), (c) Time evolution of the fraction of chromatin contacts (red) and the fraction of marked sites (blue) along representative simulation trajectories initialized from a state with zero histone marks and chromatin contacts in the fast [$k_c = 10^3$ (a)] and slow [$k_c = 10^{-1}$ (c)] chromatin regimes. (b), (d) The negative logarithm of the steady state distributions as a function of the fraction of marked sites and the fraction of chromatin contacts for $k_c = 10^3$ (b) and $k_c = 10^{-1}$ (c). We hold fixed $\mathbf{N} = 40$, $\lambda = 0.01$, $\epsilon = -2.5$.

contacts [Fig. 2(a)]. However, as contacts build, they endow the system with greater cooperativity and facilitate the spreading of marks through the recruited conversion pathway [Fig. 2(a)]. Moreover, since marks confer attraction between sites, their establishment drives further collapse of the chromatin structure, and both contacts and marks increase in concert, culminating in the formation of the collapsed marked state.

We computed the steady-state probability distributions as a function of \bar{n} and \bar{q} , i.e., $\mathbb{P}_{\text{ss}}(\bar{n}, \bar{q})$ to examine the long-time behaviors of this model. The negative logarithm of this distribution, which can be interpreted as a pseudopotential quantifying the landscape of the stochastic system [80,100–104], is shown in Fig. 2(b). Two distinct steady states, a collapsed marked state and an open unmarked state resembling heterochromatin and euchromatin, respectively, are evident. The bistable behavior is consistent with the two-state switching kinetics shown in Fig. 2(a). Therefore, our model produces steady states that naturally account for changes in chromatin organization upon changing histone modifications.

Since the precise value of chromatin dynamics is affected by a multitude of factors, such as the specifics of the polymer model and the environment the chromatin is embedded in, we modulated k_c from 10^3 to 10^{-1} to explore the phenomenology of the system. Strikingly, we observed signatures of a dynamical phase transition. Figure 3(a) shows the negative logarithm of the steady-state probability distributions as a function of the fraction of sites marked. The result from a model neglecting explicit dynamics of chromatin contacts by setting $q_{ij} = 1 \forall i, j \in [1, \mathbf{N}] \forall t$ is included for comparison.

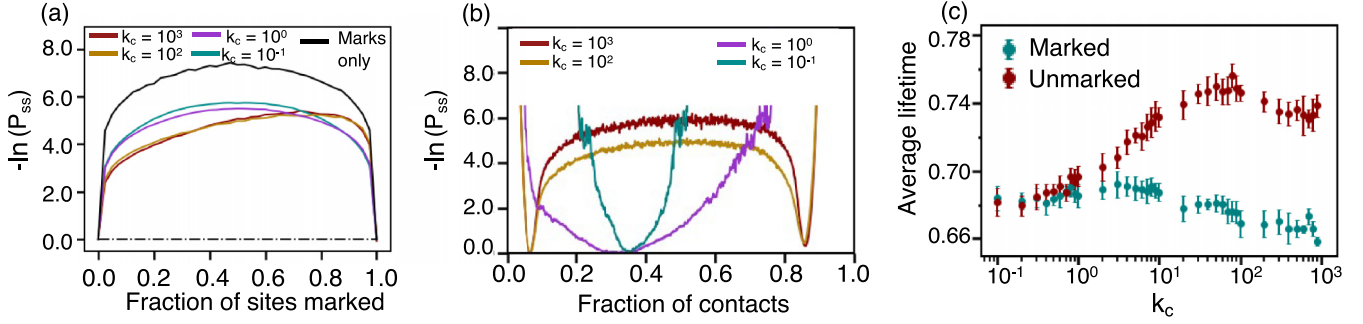


FIG. 3. Coupling between histone marks and chromatin contacts introduces an asymmetry in the epigenetic landscape and stabilizes euchromatin in the fast chromatin regime. (a) Negative logarithm of the steady-state distribution for the fraction of marked nucleosomes computed with $k_c = 10^3$ (red), $k_c = 10^2$ (yellow), $k_c = 10^0$ (purple), and $k_c = 10^{-1}$ (cyan). The result from a mark-only system without explicit chromatin conformational dynamics with $q_{ij} = 1 \forall i, j$ is provided as a reference (black). (b) Negative logarithm of the steady state distribution for the fraction of contacts made computed with $k_c = 10^3$ (red), $k_c = 10^2$ (yellow), $k_c = 10^0$ (purple), and $k_c = 10^{-1}$ (cyan). (c) Variation in the average lifetime of marked (cyan) and unmarked states (red) with the basal chromatin contact rate constant k_c . We hold fixed $N = 40$, $\lambda = 0.01$, $\epsilon = -2.5$.

As the reactions for histone marks are symmetric by design, the steady-state distribution is symmetric in the mark-only model. In Fig. 3(a), we note an asymmetry in the landscape at high $k_c = 10^3$, and the entire landscape is tilted towards the unmarked state. Strikingly, this asymmetry vanishes below a critical value for k_c , denoted as k_c^o . Similarly, we plot the negative logarithm of the steady-state probability distributions as a function of the fraction of contacts made in Fig. 3(b) and note that the landscape transitions from a bistable regime at high k_c to monostable at low k_c .

After the transition, the system's kinetic behavior deviates significantly from those shown in Figs. 2(a) and 2(b). As an illustrative example, we show a simulation trajectory with $k_c = 10^{-1}$ in Figs. 2(c) and 2(d), but similar trends can be expected for other values below k_c^o . While the histone marks transition between completely marked and unmarked states, as in the fast chromatin case, chromatin contacts vary much slower. Consequently, the intimate coupling between structure and sequence has disappeared. This is clear at the beginning of the trajectory, where the formation of even only a handful of non-backbone contacts seeds the spread of marks and supports cooperative transitions [Fig. 2(c)]. After the initial equilibration ($\approx 10^3 \tau$), the dynamics occur on a network with relatively fixed connectivities for the duration of the simulated trajectory ($\approx 10^5 \tau$). This is reflected in the steady-state behavior plotted in Fig. 2(d), as the slow chromatin regime exhibits a partially collapsed marked and a partially collapsed unmarked state.

To further our understanding of the dynamical system, we determined the lifetime of both marked and unmarked states by partitioning the simulation trajectories into the two states. As shown in Fig. 3(c), while the lifetime of marked states remains largely unchanged, the lifetime of unmarked states increases significantly as k_c increases. For small k_c , transitions between marked and unmarked states happen at rates much faster than the chromatin structural relaxation and are dictated mainly by the symmetric reaction network, producing comparable average lifetimes for both states. As chromatin contacts become more responsive to histone modifications at larger k_c , fewer contacts are expected for the unmarked states. In contrast, more will form for the marked one, driving the monostability to bistability transition [Fig. 3(a)]. The decrease

in contacts makes transitioning out of the unmarked state harder due to a lack of recruited conversions, leading to the observed increase in lifetime. On the other hand, the enhanced presence of contacts for the marked state facilitates cooperative reactions that erase the marks. The imbalance between the lifetimes of steady states produces the asymmetry in the landscape seen in Fig. 3(a). We point out that the existence of the dynamical phase transition and the qualitative behavior of the steady states in the two regimes are insensitive to the parameters of the model, including ϵ [Figs. 4(a)–4(c)] and λ [Figs. 5(a)–5(c)].

B. A mean-field expression for the contact space Hamiltonian

In the previous section, we used an Ising-like Hamiltonian to describe the stochastic transition of various contacts in chromatin. To examine whether our findings are sensitive to the functional form and parameters in the Hamiltonian, we next introduce a mean-field expression for the free energy of total contacts in the system, $\mathcal{F}(\bar{q})$. We designed the mean-field expression to capture two prominent features of polymer systems: (1) In the absence of marks, the free energy has a singular minima which corresponds to entropically favored configuration with few contacts (low \bar{q}). (2) As we titrate marks into the system the self-attraction between marked sites results in a secondary minima in the free energy corresponding to a more collapsed configuration (high \bar{q}). A simple example would be to construct $\mathcal{F}(\bar{q})$ as a quartic polynomial over $[0,1]$, where $\mathcal{F} = \sum_{r=0}^4 a_r \bar{q}^r + \epsilon_{ij} q_{ij}$, where a_r are the polynomial coefficients of \bar{q}^r , and ϵ_{ij} is a small attraction between two marked sites (i, j). One choice of parameters for this quartic polynomial is $a_0 = 0$, $a_1 = 150.0$, $a_2 = 664.043$, $a_3 = -6312.1$, $a_4 = 15000.0$, $\epsilon = -0.55$. However, we do not anticipate our results to be sensitive to these specific parameter values as long as conditions (1) and (2) outlined previously are met.

We again performed stochastic simulations for the reaction network using an implementation of the Gillespie stochastic simulation algorithm [98]. The rate for contact breaking and formation for a pair of nucleosomes (i, j) was again defined as $k_c \exp(-\beta \epsilon n_i n_j)$ and $k_c \exp(-\beta \Delta \mathcal{H})$, respectively. Now

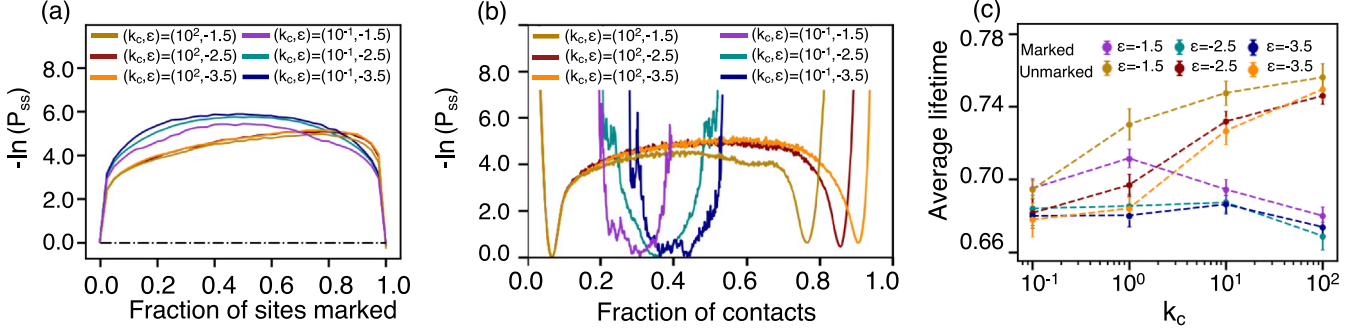


FIG. 4. The existence of the dynamical phase transition and the qualitative behavior of the steady states in the two regimes is insensitive to the parameters of the model. For $N = 40$ bead system and fixed $\lambda = 0.01$, qualitatively similar results to Fig. 3 can be recovered for different ϵ values. (a) Negative logarithm of the steady-state distribution for the fraction of marked nucleosomes computed with $(k_c, \epsilon) = (10^2, -1.5)$ (yellow), $(k_c, \epsilon) = (10^{-1}, -1.5)$ (purple), $(k_c, \epsilon) = (10^2, -2.5)$ (red), $(k_c, \epsilon) = (10^{-1}, -2.5)$ (cyan), $(k_c, \epsilon) = (10^2, -3.5)$ (orange), and $(k_c, \epsilon) = (10^{-1}, -3.5)$ (blue). (b) Negative logarithm of the steady-state distribution for the fraction of contacts made computed with $(k_c, \epsilon) = (10^2, -1.5)$ (yellow), $(k_c, \epsilon) = (10^{-1}, -1.5)$ (purple), $(k_c, \epsilon) = (10^2, -2.5)$ (red), $(k_c, \epsilon) = (10^{-1}, -2.5)$ (cyan), $(k_c, \epsilon) = (10^2, -3.5)$ (orange), and $(k_c, \epsilon) = (10^{-1}, -3.5)$ (blue). (c) Variation in the average lifetime of marked states for $\epsilon = -1.5$ (purple), $\epsilon = -2.5$ (cyan), $\epsilon = -3.5$ (blue), and unmarked states for $\epsilon = -1.5$ (yellow), $\epsilon = -2.5$ (red), $\epsilon = -3.5$ (orange), with the basal chromatin contact rate constant k_c .

$\mathcal{H}(\bar{q})$ is defined as $\mathcal{H}(\bar{q}) \equiv \sum_{r=0}^4 a_r \bar{q}^r + \ln \left(\binom{M}{\bar{q}M} \right)$. The second term is needed in the microscopic model to account for the degeneracy in different configurations that yield the same \bar{q} so the macroscopic expression for \mathcal{F} simplifies to a simple quartic polynomial. Simulations were carried out for $N = 40$ ($M = 741$) sites. In Fig. 6, we recover qualitatively similar results to the ones demonstrated in Figs. 2–5. Therefore, the dynamical phase transition in this paper is also insensitive to the explicit form of the Hamiltonian defined in Eq. (3), indicating that the results presented are both robust and of general interest.

C. An analytically tractable phenomenological model with coupled structure and sequence changes

In the full kinetic model, we found that the transition from the monostable to bistable regime in the probability of

steady-state distribution of contacts and the concomitant emergence of asymmetry in the average lifetimes of the marked and unmarked state begins to emerge around $k_c^o \sim 1$, which corresponds to a timescale of 1 h for nucleosome diffusion. While this number may seem too slow compared to experimental values on the order of seconds [92], it does not immediately exclude the biological relevance of the dynamical phase transition. Though the existence of this transition is insensitive to model details, the numerical value for k_c^o is not. For example, as shown in Fig. 7, k_c^o can increase by order of magnitude as we change the system size, N , from 40 to 100. Furthermore, the specific Hamiltonian chosen here, parameterized with homopolymer simulations, may be insufficient for reproducing complex viscoelastic behavior of chromatin *in vivo*, underestimating k_c^o . To provide more insight into the determining factors of the dynamical phase transition, in this section, we introduce a phenomenological model that captures

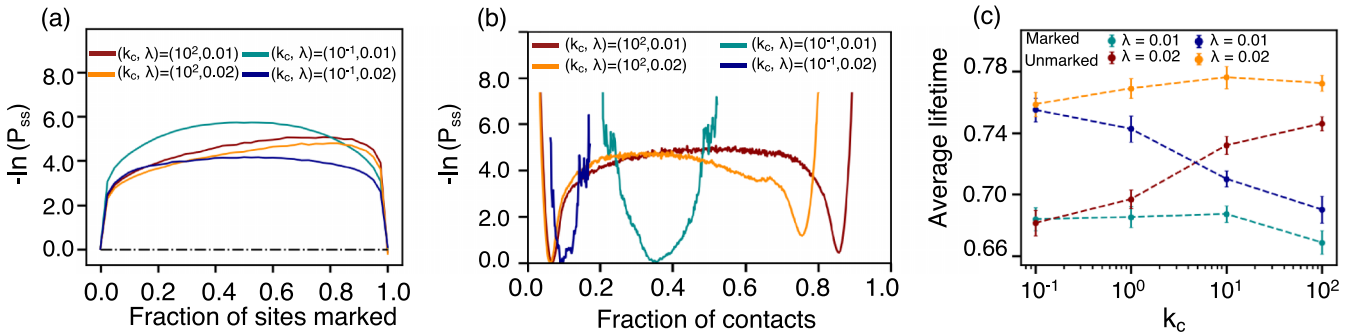


FIG. 5. The dynamical phase transition and the qualitative behavior of the steady state persists if we hold $\epsilon = -2.5$ fixed and vary λ and for $N = 40$ bead system, qualitatively similar results to Fig. 3 can be recovered for different λ values. (a) Negative logarithm of the steady state distribution for the fraction of marked nucleosomes computed with $(k_c, \lambda) = (10^2, 0.01)$ (red), $(k_c, \lambda) = (10^{-1}, 0.01)$ (cyan), $(k_c, \lambda) = (10^2, 0.02)$ (orange), and $(k_c, \lambda) = (10^{-1}, 0.02)$ (blue). (b) Negative logarithm of the steady-state distribution for the fraction of contacts made computed with $(k_c, \lambda) = (10^2, 0.01)$ (red), $(k_c, \lambda) = (10^{-1}, 0.01)$ (cyan), $(k_c, \lambda) = (10^2, 0.02)$ (orange), and $(k_c, \lambda) = (10^{-1}, 0.02)$ (blue). (c) Variation in the average lifetime of marked states for $\lambda = 0.01$ (cyan), $\lambda = 0.02$ (blue) and unmarked states for $\lambda = 0.01$ (red), $\lambda = 0.02$ (orange) with the basal chromatin contact rate constant k_c .

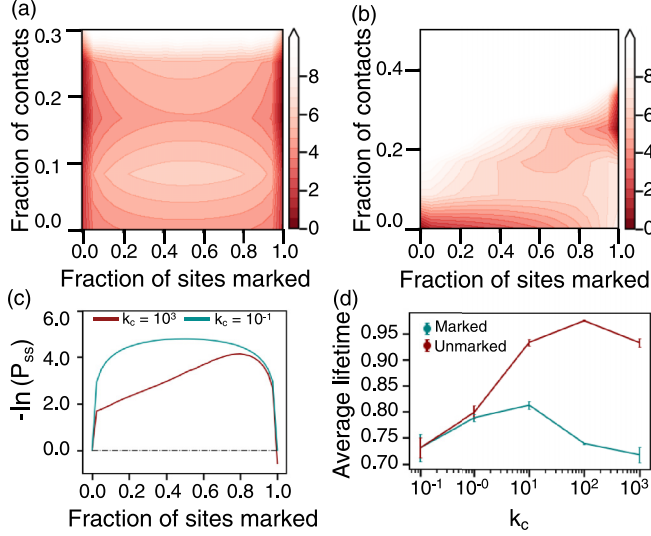


FIG. 6. A minimal mean-field model recapitulates the main results presented in Figs. 2–5 for $N = 40$ bead system. Steady state probability distributions for the (a) slow chromatin regime with $k_c = 10^{-1}$ and (b) fast chromatin regime with $k_c = 10^3$. (c) $-\ln(\mathbb{P}_{ss})$ for marks plotted as a function of the fraction of marked sites for $k_c = 10^3$ (red) and $k_c = 10^{-1}$ (cyan). (d) Variation in average lifetime of marked (cyan) and unmarked states (red) with k_c .

the essence of the full kinetic model but is now analytically tractable.

The model presented herein captures the stochastic fluctuations in chromatin contacts and histone marks as in the full kinetic model presented prior and also accounts for the coupling between changes in chromatin structure and sequence (Fig. 8). We treat contact formation (and breaking) like a birth-death process. Furthermore, we approximate the marks as a two-state system, transitioning between fully marked ($s = 0$) and fully unmarked ($s = 1$) states. The dynamics of this analytical model can be described by the following master equation:

$$\begin{aligned} \partial_t \mathbf{P}(n_q, t) = & g \mathbb{1} \{ \mathbf{P}(n_q - 1, t) - \mathbf{P}(n_q, t) \} \\ & + \begin{pmatrix} k_1 & 0 \\ 0 & k_0 \end{pmatrix} \{ (n_q + 1) \mathbf{P}(n_q + 1, t) - n_q \mathbf{P}(n_q, t) \} \\ & + \begin{pmatrix} -h & f \\ h & -f \end{pmatrix} \mathbf{P}(n_q, t), \end{aligned} \quad (4)$$

where $\mathbf{P}(n_q, t) = \begin{pmatrix} P_1(n_q, t) \\ P_0(n_q, t) \end{pmatrix}$ represents the probability of finding the system in fully marked ($s = 1$) or unmarked ($s = 0$) states with total n_q number of chromatin contacts. k_s and g represent the rate of contact breaking or formation. The transition rates between marked and unmarked states, h and f , are assumed equal to $k_m \exp(-\Delta V(\bar{n}, \bar{q}))$. $V(\bar{n}, \bar{q})$ acts as a pseudopotential and is derived based on an analytical theory of epigenetic stability [24]. The pseudopotential accounts for both stochastic fluctuations of histone marks and the impact of chromatin structures.

The transition from $s = 0$ to $s = 1$ occurs with rate $h(\bar{n}, \bar{q}) = k_m \exp(-(V(\bar{n} = 0.5, \bar{q}) - V(\bar{n} = 1, \bar{q})))$, while the transition from $s = 1$ to $s = 0$ occurs with rate

$f(\bar{n}, \bar{q}) = k_m \exp(-(V(\bar{n} = 0.5, \bar{q}) - V(\bar{n} = 0, \bar{q})))$. We estimate $k_m \sim N^{-1} c_n$, where c_n is the rate for random removal of histone modifications as introduced in the text prior.

Following Ref. [24], we derive the pseudopotential $V(\bar{n}, \bar{q})$ (5). The details of the derivation are outlined in Appendix B:

$$V(\bar{n}) = 2N\bar{n}(1 - \bar{n}) + \left(1 - \frac{4N}{Fq^2} \right) \ln[Fq^2\bar{n}(1 - \bar{n}) + 1]. \quad (5)$$

Following a second quantization approach [15,20], we rewrite the master equation as an imaginary time Schrödinger equation:

$$\partial_t |\Psi(t)\rangle = \Omega |\Psi(t)\rangle. \quad (6)$$

Here, the state vector $|\Psi(t)\rangle = \begin{pmatrix} \Psi_1(t) \\ \Psi_0(t) \end{pmatrix}$ is a superposition of all possible configurations weighted with their corresponding probabilities such that $\Psi_i(t) = \sum_{n_q} P_i(\{n_q\}; t) |n_q\rangle$ for $s = 0, 1$. The Hamiltonian operator Ω is defined as

$$\Omega = g(a^\dagger - 1) + k(a - a^\dagger a) + \begin{pmatrix} -h(\bar{n}, \bar{q}) & f(\bar{n}, \bar{q}) \\ h(\bar{n}, \bar{q}) & -f(\bar{n}, \bar{q}) \end{pmatrix}. \quad (7)$$

The operator a^\dagger serves to create a contact, i.e., it acts on a state with n_q contacts ($|n_q\rangle$), $a^\dagger |n_q\rangle = |n_q + 1\rangle$. Similarly, a serves to decrement contacts, $a |n_q\rangle = n_q |n_q - 1\rangle$. Correspondingly, $a^\dagger a |n_q\rangle \equiv \hat{n}_q |n_q\rangle = n_q |n_q\rangle$, simply returning the number of contacts in a given state.

We note that the imaginary time Schrödinger equation is equivalent to the functional variation of the following action Γ with respect to Φ , i.e., $\frac{\delta \Gamma}{\delta \Phi} = 0$, where $\Gamma = \int dt \langle \Phi | \partial_t - \Omega | \Psi \rangle$. Thus, for appropriate trial functions for Φ and Ψ parameterized with $\alpha_L = \alpha_L^1, \alpha_L^2, \dots, \alpha_L^K$ and $\alpha_R = \alpha_R^1, \alpha_R^2, \dots, \alpha_R^K$, minimizing the action leads to a set of ordinary differential equations:

$$\sum_{l=1}^K \left[\left\langle \frac{\partial \Phi}{\partial \alpha_L^l} \middle| \frac{\partial \Psi}{\partial \alpha_R^l} \right\rangle \frac{d\alpha_R^l}{dt} - \left\langle \frac{\partial \Phi}{\partial \alpha_L^m} \middle| \Omega | \Psi \right\rangle \right]_{\alpha_L^m=0} = 0. \quad (8)$$

Using a variational *ansatz* we obtain the following set of variational equations:

$$\frac{dc_1}{dt} = c_0 \langle f(\hat{n}_q) \rangle_0 - c_1 \langle h(\hat{n}_q) \rangle_1, \quad (9a)$$

$$\frac{d\bar{q}_1}{dt} c_1 + \frac{d\bar{q}_1}{dt} c_1 = c_1 g_1 - c_1 k_1 \bar{q}_1 + c_0 \langle f(\hat{n}_q) \hat{n}_q \rangle_0 \quad (9b)$$

$$- c_1 \langle h(\hat{n}_q) \hat{n}_q \rangle_1, \quad (9c)$$

$$\frac{dc_0}{dt} \bar{q}_0 + \frac{d\bar{q}_0}{dt} c_0 = c_0 g_0 - c_0 k_0 \bar{q}_0 - c_0 \langle f(\hat{n}_q) \hat{n}_q \rangle_0 \quad (9d)$$

$$+ c_1 \langle h(\hat{n}_q) \hat{n}_q \rangle_1. \quad (9e)$$

The angular brackets represent averaging over number of contacts using a Poisson distribution, i.e., $\langle \cdot \rangle_s = \sum_{n_q} \frac{e^{-\bar{q}_s} \bar{q}_s^{n_q}}{n_q!} \bar{q}_s^{n_q}$. We also make a simplifying assumption that $\langle F(x) \rangle \approx F(\langle x \rangle)$. We assume steady-state solutions of Eqs. (9) take the form $\bar{q}_1 = \bar{q}^h + \delta$ and $\bar{q}_0 = \bar{q}^h - \delta$, where $\bar{q}^h = 2g/(k_1 + k_0)$. Plugging this into Eqs. (9), we obtain

$$g - k_1(\bar{q}^h + \delta) + 2\langle h(\bar{q}^h + \delta) \rangle \delta = 0. \quad (10)$$

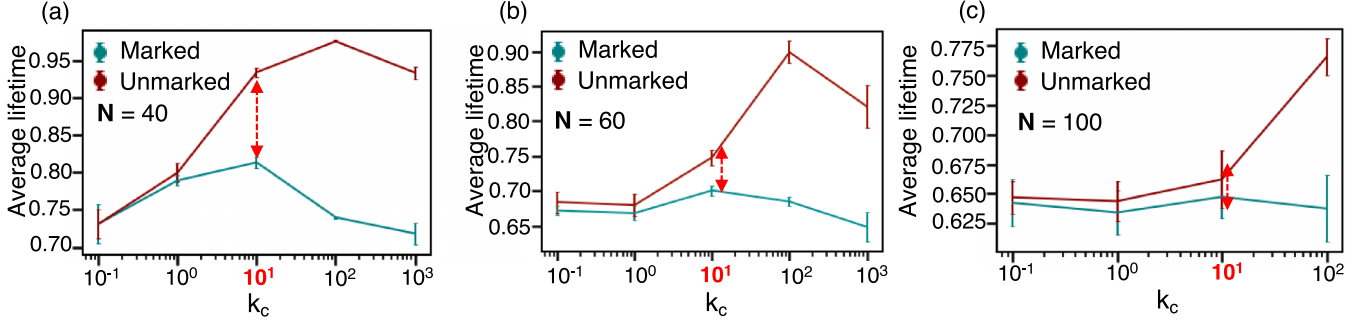


FIG. 7. k_c^o increases with system size. We plot the average lifetimes in the marked (red) and unmarked states (cyan) against k_c for systems of size (a) $N = 40$, (b) $N = 60$, and (c) $N = 100$. We note that at $k_c = 10$, the smaller ($N = 40$) system is already asymmetric, however, there is no appreciable difference in the average lifetimes at $k_c = 10$ for the larger ($N = 100$) system. Simulations performed using the mean-field approach to the polymer model discussed in Sec. II B and Fig. 6.

We linearize $h(\bar{q}^h + \delta)$ around δ , and then solve for δ :

$$\delta = \frac{\frac{2gk_1}{k_1+k_0} - g}{-k_1 + 2e^{N/2} \left(1 + \frac{Fg^2}{(k_1+k_0)^2}\right)^{\frac{N(k_1+k_0)^2}{Fg^2} - 1} k_m}. \quad (11)$$

Finally, we observe $\delta \rightarrow 0$ as $g/k_m \rightarrow 0$ and $\delta \rightarrow \infty$ as $g/k_m \rightarrow \infty$. In the former case, when the rate of contact creation is low relative to mark turnover, we are in the monostable regime. However, as the rate of contact formation is appreciably large then we transition to a bistable regime.

Therefore, the phenomenological model reproduces the dynamical phase transition as well. Importantly, it clarifies that the rate of contact formation (birth rate g) determines the transition between the two regimes. g can be impacted by nucleosome diffusion (k_c), polymer topology, and the nucleoplasm. Using the condition $\bar{q}^h/\delta \gg 1$, we can

bound the transition birth rate, $(g^o)^2 \lesssim \frac{4e^{N/2}(k_0+k_1)^2 k_m}{F(3k_1-k_0)}$. For a birth-death process with n_q contacts, the probability of $P(n_q - 1|n_q) \sim \left(\frac{k_1+k_0}{g^o + \frac{k_1+k_0}{2}}\right)$. We approximate $k_1 \sim e^{-2.5}$, $k_0 \sim 1$, $N \sim 40$, $k_m \sim N^{-1}c_n$, $F \sim 10^2$. We estimate $c_n \sim 0.6 \text{ h}^{-1}$. Using these, we estimate the lifetime of contacts for near the critical point $\left(\frac{k_1+k_0}{g^o + \frac{k_1+k_0}{2}}\right)^{-1} \sim 10 \text{ s}$.

III. CONCLUSIONS

In summary, our paper has demonstrated that incorporating the interplay between chromatin structural dynamics and histone modification kinetics can give rise to a dynamical phase transition. We verified the validity of this transition by reproducing it in multiple models: a comprehensive kinetic model encompassing microscopic chromatin contacts, a mean-field model, and a phenomenological model. This extensive validation underscores the robustness of our findings. Moreover, the behavior observed in the fast chromatin dynamics limit aligns with well-established observations regarding the influence of histone modifications on chromatin structure. Additionally, experimental evidence for slow chromatin relaxation further highlights the significance of our results in the opposite limit [79,105]. By introducing the concept of a dynamical phase transition, we provide a cohesive framework that reconciles observations across different limits. Future experiments specifically designed to explore chromatin viscoelasticity under various conditions hold the potential to validate our theoretical predictions further. Moreover, some of the methods and ideas are broadly applicable to the study of dynamical processes and problems, in general, where there exists a coupling between 3D network structure and 1D sequence information, and where there is the presence of dynamical asymmetry in the relaxation rates for the two.

The computer code for carrying out the simulations discussed in this paper has been made available on GitHub [106].

ACKNOWLEDGMENTS

This work was supported by the National Institutes of Health (Grant No. R35GM133580).

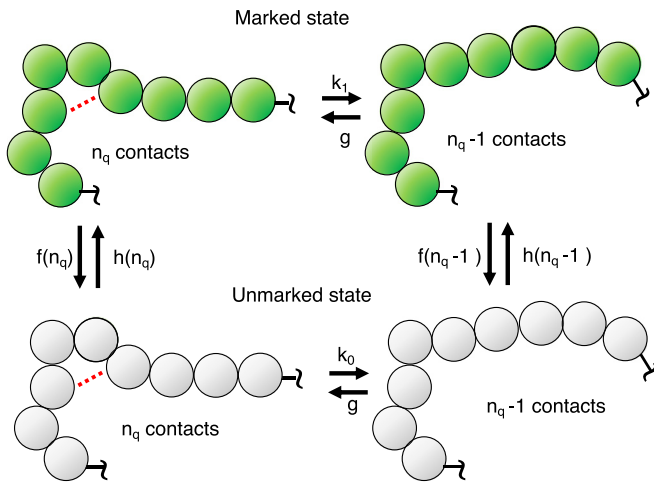


FIG. 8. A schematic illustration of the salient features of a phenomenological model described by Eq. (4). The system can transition between fully marked (green) and fully unmarked (grey) states with rate $f(n_q)$, $h(n_q)$, respectively. In either state, precise topological, polymeric effects are ignored, and the number of contacts (n_q) is incremented at rate g . Furthermore, n_q is decremented at rate k_1 , k_0 in the fully marked and unmarked states. $k_1 < k_0$ accounts for the attraction conferred between marked nucleosomes.

APPENDIX A: PARAMETERIZING THE FREE ENERGY FUNCTIONAL OF CHROMATIN CONFORMATIONS IN THE CONTACT SPACE

For efficient simulations across a wide range of timescales, we consider chromatin conformational dynamics in the contact space. For a chromatin segment with N nucleosomes, the total set of contacts is represented with a vector of size \mathbf{M} , $\mathbf{q}(t) \equiv \{q_{ij}(t)\}$ for $i, j \in [1, N]$ and $j - i > 1$. The binary variables $q_{ij} \in \{0, 1\}$ denote the presence (or absence) of 3D contacts between a pair of nucleosomes (i, j) . We assume that neighboring nucleosomes are always in contact, i.e., $q_{i,i+1} \equiv 1$ and $\mathbf{M} = \mathbf{N}(\mathbf{N} - 1)/2 - (\mathbf{N} - 1)$.

Recall that the free-energy functional in contact space is given by

$$\begin{aligned} \mathcal{H}(\mathbf{q}) = & \sum_{ij} h_{ij} q_{ij} + \sum_{ijkl} J_{ijkl} q_{ij} q_{kl} \\ & + \lambda \sum_{ij} q_{ij} \left(\sum_{t \neq i, j} q_{it} + \sum_{t \neq j, i} q_{tj} \right). \end{aligned} \quad (\text{A1})$$

The linear terms h_{ij} incorporate the entropic penalty of loop formation. We enforce translational symmetry such that contacts with the same sequence separation share identical penalties [88], i.e., $h_{ij} = h_{kl}$ whenever $j - i = l - k$. The correlation between contacts (i, j) and (k, l) , which is caused by the polymer's topology, is accounted for by J_{ijkl} . Without loss of generality, the J indices are ordered such that $k_1 \equiv j - i \leq l - k \equiv k_2$. Whenever $k_1 = k_2$, we additionally require $l > j$. Topologically equivalent contact pairs can be identified by also defining $L \equiv l - j$ [89,90]. Naturally, the topology-driven correlations are identical for topologically equivalent contact pairs. Therefore, we assign identical J values to all contact pairs with identical k_1 , k_2 , and L values [89,90]. Furthermore, we set $J_{ijkl} = 0$ for contacts with nonoverlapping loops, which occur whenever $j \leq k$ or $l \leq i$, because the polymer's topology has no effect on these contacts' correlation [89,90]. The third term accounts for the excluded volume effect that limits the number of contacts a given nucleosome can form.

We determined the parameters in Eq. (A1) such that the free-energy functional accurately describes the conformational distribution of polymers. As detailed below, the conformational distribution was produced with molecular dynamics simulations, and we used the pseudolikelihood approach for efficient parameter inference.

Note that each J_{ijkl} parameter affects the total energy only when both of its corresponding contacts are formed. Therefore, negative J values favor contact formation. Meanwhile, the optimization scheme discussed in Appendix A2 yields a model with many more negative than positive J values. Additionally, the negative J values are larger in magnitude than the positive J values. This biases the system towards states in which many beads are involved with an unphysically large number of contacts. The third term of the Hamiltonian corrects this effect. This second-order correction term penalizes individual beads forming multiple contacts. Physically, this represents the excluded volume effect. A λ value of 0.01 was sufficient to prevent the polymer collapse.

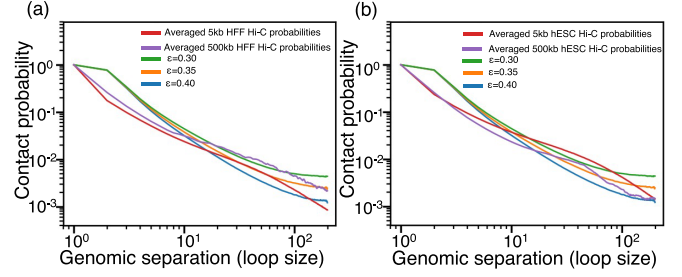


FIG. 9. For most loop sizes relevant to this study, the loop size-averaged contact probabilities associated with the three polymer models agree with Hi-C data representing the first chromosome of (a) human foreskin fibroblasts (HFF) and (b) human embryonic stem cells (hESC) cells at 5 and 500 kb resolution. Plotting the contact probabilities against their loop size, $|j - i|$, highlights the influence of topological constraints in each system.

1. Polymer conformations from molecular dynamics simulations

We performed three independent molecular dynamics simulations to produce three conformational ensembles of polymers. The monomers are connected to nearest neighbors with the finite extensible nonlinear elastic (FENE) potential:

$$\begin{aligned} u_{\text{bond}}(r_{i,i+1}) = & -\frac{1}{2} K R_0^2 \ln \left[1 - \left(\frac{r_{i,i+1}}{R_0} \right)^2 \right], \\ K_b = & 30\epsilon, R_0 = 1.5\sigma. \end{aligned} \quad (\text{A2})$$

The Lennard-Jones (LJ) potential was applied between all monomer pairs

$$U_{\text{wall}}(r) = \begin{cases} 4\epsilon_{\text{LJ}} \left[\left(\frac{\sigma}{r} \right)^{12} - \left(\frac{\sigma}{r} \right)^6 \right] + E_{\text{cut}}, & r < r_c \\ 0, & \text{otherwise,} \end{cases} \quad (\text{A3})$$

where E_{cut} is the energy of the LJ potential at the cutoff distance $r_c = 2.6\sigma$. We chose ϵ_{LJ} as 0.35 for the LJ potential because it creates a sequence separation dependence for contact probabilities similar to that expected in chromatin systems *in vivo* [91]. Figure 9 illustrates this, showing the relationship between contact probability and sequence separation for each of the homopolymer models and for Hi-C data from (a) human foreskin fibroblasts (HFFs) and (b) human embryonic stem cells (hESCs). Each Hi-C contact probability represents the average of all contact probabilities in the first chromosome with the same sequence separation, so the plot illustrates nonspecific effects; similarly, homopolymer contact probabilities were averaged for monomer pairs separated by the same number of bonds. In addition, we simulated homopolymer models using $\epsilon_{\text{LJ}} = 0.3$ and $\epsilon_{\text{LJ}} = 0.4$ to obtain two additional sets of homopolymer conformations that remain biologically plausible while being qualitatively distinct; these sets improve the result of our pseudolikelihood maximization procedure discussed in the next subsection. The simulated polymer is 500 beads in length, and only the conformations of the central 40 beads were recorded. Simulating a longer polymer avoids potential edge effects that might produce different statistics for polymer beads at the boundary.

The LAMMPS software package [107] was used to perform the simulations using reduced units and shrink-wrapping boundary conditions with a time step of 0.005. Langevin dynamics with a damping parameter of 10 were used to main-

tain the temperature. Temperature replica exchange was used with seven temperatures evenly spaced from 0.7 to 1.3, and data was collected from the replica with $T = 1.0$. Exchanges were performed every 100th timestep, and configurations were collected once every 5000 time step over one billion total time steps. This yields 200 000 configurations for each of the three homopolymers.

2. Parameter optimization with the pseudolikelihood approach

The model parameters h_{ij} and J_{ijkl} were learned using a pseudolikelihood maximization approach developed in pre-

vious work [93]. This approach adjusts the parameters to optimize the probability, or likelihood, of the conformations from a reference ensemble. From the 3D structures in Cartesian space obtained using molecular dynamics simulations, we obtained a list of contacts between monomer pairs using a distance cutoff of 1.707σ . This conversion produces three ensembles of polymer conformations in the contact space, denoted as \mathbb{B}_1 , \mathbb{B}_2 , and \mathbb{B}_3 , which were used in pseudolikelihood optimization.

The function used for parameter optimization is defined as

$$\begin{aligned} \ell_{\text{pseudo},\mathbb{B}}(\mathbf{h}, \mathbf{J}, \Delta\mathbf{h}) = & \sum_{b \in \mathbb{B}_1} \sum_{(i,j)} \ln \left[\frac{1}{1 + \exp((2q_{ij} - 1)(h_{ij} + \Delta h_1 + \sum_{kl} J_{ijkl} q_{kl}^{(b)}))} \right] \\ & + \sum_{b \in \mathbb{B}_2} \sum_{(i,j)} \ln \left[\frac{1}{1 + \exp((2q_{ij} - 1)(h_{ij} + \Delta h_2 + \sum_{kl} J_{ijkl} q_{kl}^{(b)}))} \right] \\ & + \sum_{b \in \mathbb{B}_3} \sum_{(i,j)} \ln \left[\frac{1}{1 + \exp((2q_{ij} - 1)(h_{ij} + \Delta h_3 + \sum_{kl} J_{ijkl} q_{kl}^{(b)}))} \right] \end{aligned} \quad (\text{A4})$$

Here, $\mathbf{h}(\mathbf{J})$ is the model's full set of h_{ij} (J_{ijkl}) parameters. The three terms on the right side correspond to the total pseudolikelihood of the energy function defined in Eq. (A1) over the configurations from the three ensembles. Since the molecular dynamics simulations used to produce the three ensembles differ in the nonbonded interaction energy, we introduced $\Delta\mathbf{h} = \{\Delta h_1, \Delta h_2, \Delta h_3\}$ to account for the difference. Δh_1 , corresponding to $\varepsilon_{\text{LJ}} = 0.35$, was fixed at 0. Our use of three conformational ensembles with different degrees of polymer collapse provides a wide variety of conformations essential for probing the correlation between contact pairs.

As mentioned in the main text, the first-order parameter h_{ij} accounts for the entropic penalty associated with forming contact (i, j) . In addition, it includes the contact potential associated with the interaction between i and j in the homopolymer, so shifting the well depth associated with each Lennard-Jones potential, ε_{LJ} , causes a constant shift in all h_{ij} . $\Delta h_\varepsilon \in \Delta\mathbf{h}$ accounts for these shifts, and we fixed $\Delta h_1 = 0$ so the computed h parameters correspond to the simulation with $\varepsilon_{\text{LJ}} = 0.35$. We related h to the homopolymer parameterized by $\varepsilon_{\text{LJ}} = 0.35$ because the sequence-separation dependence of contact probabilities in that model agree with the probabilities observed in chromatin systems *in vivo* [91]. Meanwhile, the supporting simulations use ε_{LJ} that differ from this biologically accurate parametrization by the small $\Delta\varepsilon_{\text{LJ}} = \pm 0.05$ to ensure that the resulting sets of conformations remain biologically plausible while providing qualitatively distinct sets of conformations [Fig. 10(a)].

On the other hand, J accounts for the correlation between contacts, which primarily depends on connectivity and excluded volume effects [89,90]. The former is independent of ε_{LJ} , and the latter is negligibly affected by it. Consequently, J is unaffected by the choice of ε_{LJ} , and all models share the same J values. Therefore, using PLM to infer the Ising-like parameters of all three models simultaneously provides

additional information regarding first- and higher-order processes, encouraging h and J to capture the intended entropic effects.

Additional regularization was introduced to ensure the robustness of parameter optimization, leading to the final objective function

$$\ell_{\mathbb{B}}(\mathbf{h}, \mathbf{J}, \Delta\mathbf{h}) = \ell_{\text{pseudo},\mathbb{B}} + \gamma \sum_{ijkl} J_{ijkl}^2, \quad (\text{A5})$$

with γ set to 0.6.

The function was optimized with the limited-memory Broyden–Fletcher–Goldfarb–Shannon with bound variables (L-BFGS-B) algorithm using SciPy version 1.5.2. All parameters were initialized at 0.

3. Characterizing the parameterized model

In Fig. 10(a), we plot the distribution of the homopolymer's radius of gyration (R_g) within each simulated set of homopolymer conformations, i.e., the set of conformations associated with each ε value and obtained via MD simulation. For each conformation, we computed the R_g of the central 40 monomers of the polymer alone, as this is the polymer region considered by our pseudolikelihood maximization procedure. The observed distributions indicate that the homopolymer by itself is expected to be relatively open, and we reiterate that the kinetic model incorporates Ising-like parameters representing a homopolymer with $\varepsilon_{\text{LJ}} = 0.35$. We note that each set of conformations was used only once, namely, to parametrize the Ising-like representation of a homopolymer model. Afterward, the kinetic simulations discussed in the main text utilized this parametrization, which remained constant throughout; the attractions in the system that arise from nucleosome marking are introduced during the kinetic simulation and are entirely independent of the pseudolikelihood

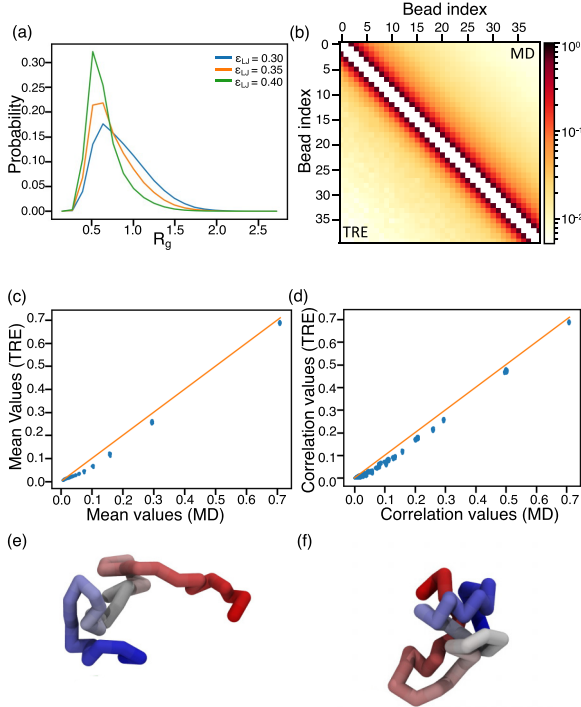


FIG. 10. Characterizing and comparing the homopolymer conformations determined via an MD simulation of the $\lambda = 0.01$ polymer model and via a temperature replica exchange (TRE) Markov chain Monte Carlo (MCMC) simulation of the Ising-like model. (a) Compactness, measured by the distribution of the homopolymer's radius of gyration (R_g), differs between models parameterized with different ε_{LJ} values in each of three MD simulations. (b), (c) The mean contact probabilities associated with the Ising-like model and computed via TRE MCMC (lower triangle, y axis) agree reasonably well with the mean contact probabilities computed from MD simulation-derived polymer conformations (upper triangle, x axis). (d) The correlation between each contact pair, defined as $\langle q_i q_j \rangle$, agrees well in both the TRE MCMC-simulated Ising-like model (y axis) and MD-simulated polymer model (x axis). Open (e) and collapsed (f) polymer conformations are shown, having R_g values of ≈ 2.01 and 0.22 , respectively. Each conformation was computed via MD simulation of the homopolymer model that uses Lennard-Jones interaction potentials with magnitude $\varepsilon_{LJ} = 0.35$.

maximization task and the specific h_{ij} and J_{ijkl} values. As to the specific ε_{LJ} values chosen in this work, the contact probabilities produced by the polymer model using $\varepsilon_{LJ} = 0.35$ agree with the sequence separation-averaged contact probabilities observed in *in vivo* chromatin systems. [See Ref. [91], which uses an identical parametrization for the homopolymer model described in its Fig. 5(a).] Therefore, the $\varepsilon_{LJ} = 0.35$ model is biologically relevant, and the supporting simulations use ε_{LJ} that differ from this biologically accurate parametrization by the small $\Delta\varepsilon_{LJ} = \pm 0.05$ to ensure that the resulting sets of conformations remain biologically plausible while still providing qualitatively distinct sets of conformations. We note a reasonable agreement between the statistics obtained from explicit molecular dynamics simulations and those reproduced by our learned model (Fig. 10). This is more than sufficient for our intended primary purpose of demonstrating that coupling between the stochastic epi-

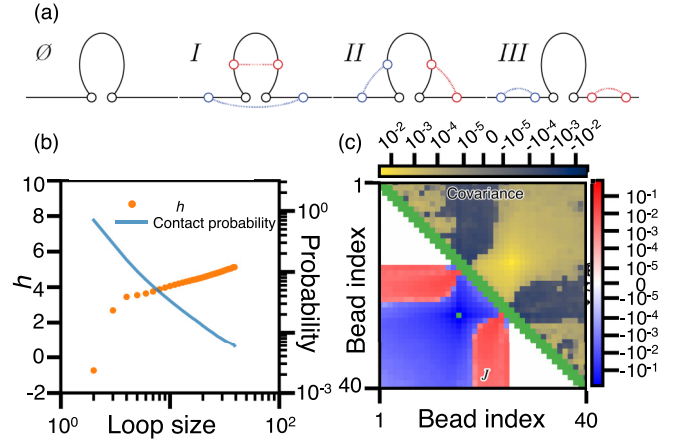


FIG. 11. The Ising-like model parameters are compared to the physical effects they capture. The MD simulation of the homopolymer using $\varepsilon = 0.35$ provided the included contact statistics. (a) Illustration of various topological relationships between loops. \emptyset illustrates the loop associated with one contact. This loop resides within or fully contains loops in region I, partially overlaps with loops in region II, and is independent of loops in region III. (b) The contact probabilities, $\langle q_{ij} \rangle$, and entropic penalties, h_{ij} , are plotted against their associated loop size, $j - i$. For visual clarity, the plot displays the average value of all $\langle q_{ij} \rangle$, corresponding to each loop size. However, as shown in the upper triangle of Fig. 10(b), they are similar to the plotted probability whose contact has the same loop size. Meanwhile, $h_{ij} \forall (i, j)$ are plotted against their associated loop size. (c) The coupling (lower triangle) and correlation (upper triangle) between contact (16,26) and all other contacts (k, l) are plotted on a two-dimensional grid. $J_{16,26,kl}$ quantifies coupling, where k and l index the x and y axis, respectively. Mirroring each interaction across the diagonal, the covariance $\langle q_{16,26} q_{kl} \rangle - \langle q_{16,26} \rangle \langle q_{kl} \rangle$ quantifies the correlation between the formation of the relevant contacts, where l and k index the x and y axis, respectively. Green indicates values that are undefined in the Ising-like model.

genetic reaction network and structure produces interesting dynamical behavior when the underlying structure relaxes on disparate timescales. The subtleties of parametrizing Ising-like models of homopolymers are the subject of other works [91].

Figure 10 includes plots that compare the first- [Figs. 10(b) and 10(c)] and second-order [Fig. 10(d)] contact statistics of the Ising-like model, obtained via a TRE MCMC simulation, to the statistics computed from the homopolymer conformations obtained via MD simulation. These plots demonstrate the quality of the parameters composing the homopolymer model.

In addition, Fig. 11 compares h and J to the MD-derived homopolymer contact statistics that illustrate the physical effects they capture. First, topological constraints cause the contact probability between beads i and j to decrease as their sequence separation, quantified by the loop size $j - i$ increases [88–90]. The left panel shows this effect, and the Ising-like model captures it by increasing h as loop size increases. Second, topological constraints couple the formation of different contacts [89,90], which we illustrate with the covariance between each pair of interactions, i.e., $C_{ijkl} \equiv$

$\langle q_{ij}q_{kl} \rangle - \langle q_{ij} \rangle \langle q_{kl} \rangle$. To visualize second-order data, the right panel considers the interaction between the contact (16,26) and all other contacts (k, l), and the grid uses k and l (lower triangle) or l and k (upper triangle) to index the x and y axis, respectively. The covariance $C_{16,26,kl}$ is positive for interactions in which one loop contains the other, negative for partially overlapping loops, and near zero for loops that don't overlap. (Chan and Dill provide a thorough description of the distinct topological conditions associated with each of these interaction types in Refs. [89,90].) Supporting these correlations, the $J_{16,26,kl}$ values (lower triangle) are negative valued for correlated contact pairs ($C_{16,26,kl} > 0$), positive valued for anticorrelated contact pairs ($C_{16,26,kl} < 0$), and zero valued for uncorrelated contact pairs ($C_{16,26,kl} \approx 0$). Green indicates values that are undefined in the Ising-like model.

APPENDIX B: DERIVING THE PSEUDO-POTENTIAL AND TRANSITION RATES

Following Ref. [24], we derive the pseudopotential $V(\bar{n}, \bar{q})$ that dictates the transition rates between marked and unmarked states. We consider $\bar{n} = \sum_i n_i/N$, the fraction of nucleosomes in the modified state. The kinetic equation for $d\bar{n} = 1/N$ is

$$\frac{d\bar{n}}{dt} = (R_+(\bar{n}) - R_-(\bar{n}))d\bar{n}, \quad (\text{B1})$$

where

$$R_+(\bar{n}) = c_r \bar{n}^2 (1 - \bar{n}) \bar{q}^2 + c_n (1 - \bar{n}), \quad (\text{B2a})$$

$$R_-(\bar{n}) = c_r \bar{n} (1 - \bar{n})^2 \bar{q}^2 + c_n \bar{n}. \quad (\text{B2b})$$

The $c_r \bar{n}^2 (1 - \bar{n}) \bar{q}^2$ term in the above equations represents the rate of recruited conversion from unmarked to marked nucleosomes. Similarly, $c_r \bar{n} (1 - \bar{n})^2 \bar{q}^2$ corresponds to recruited conversions from marked to unmarked nucleosomes. The terms proportional to c_n represent noisy conversions. c_r and c_n are the same rates introduced in the main text. For convenience, we introduce the feedback ratio $F = c_r/c_n$, the ratio of recruited to random conversions. We formulate the master equation for this system:

$$\begin{aligned} \partial_t P(\bar{n}, t) &= R_-(\bar{n} + d\bar{n})P(\bar{n} + d\bar{n}, t) \\ &\quad + R_+(\bar{n} - d\bar{n})P(\bar{n} - d\bar{n}, t) \\ &\quad - [R_+(\bar{n}) + R_-(\bar{n})]P(\bar{n}, t). \end{aligned} \quad (\text{B3})$$

We expand Eq. (B3) to second order to obtain the following Fokker-Planck equation:

$$\begin{aligned} \partial_t P &= -\frac{\partial J}{\partial \bar{n}} = -\frac{\partial}{\partial \bar{n}} \left[-\mu(\bar{n}) \frac{dU(\bar{n})}{d\bar{n}} P - \frac{\partial(D(\bar{n})P)}{\partial \bar{n}} \right] \\ &= -\frac{\partial}{\partial \bar{n}} \left[-\mu(\bar{n}) \frac{dV(\bar{n})}{d\bar{n}} P - D(\bar{n}) \frac{\partial P}{\partial \bar{n}} \right]. \end{aligned} \quad (\text{B4})$$

J in the above equation describes the probability flux, $\mu(\bar{n})$ is the mobility, and $D(\bar{n})$ is the diffusion coefficient. $V(\bar{n})$ is an effective potential that includes both drift and noise events,

defined as $\frac{dV}{d\bar{n}} = \frac{dU}{d\bar{n}} + \frac{D}{\mu} \frac{d \ln(D)}{d\bar{n}}$. The pseudopotential, $V(\bar{n})$ is obtained by expanding Eq. (B3) to second-order and comparing it with Eq. (B4). We identify the drift ($\frac{d\bar{n}}{dt} = \mu(\bar{n}) \frac{dU}{d\bar{n}}$), the pseudopotential ($V(\bar{n})$), diffusion ($D(\bar{n})$), and mobility ($\mu(\bar{n})$) as follows:

$$\left\langle \frac{d\bar{n}}{dt} \right\rangle = \frac{c_r q^2}{N} (2\bar{n} - 1) \left(\bar{n}(1 - \bar{n}) - \frac{1}{F q^2} \right), \quad (\text{B5})$$

$$V(\bar{n}) = 2N\bar{n}(1 - \bar{n}) + \left(1 - \frac{4N}{F q^2} \right) \ln[F q^2 \bar{n}(1 - \bar{n}) + 1], \quad (\text{B6})$$

$$\mu(\bar{n}) = D(\bar{n}) = \frac{c_r q^2}{2N^2} \left(\frac{1}{F q^2} + \bar{n}(1 - \bar{n}) \right). \quad (\text{B7})$$

The transition from $s = 0$ to $s = 1$ in Eq. (4) occurs with rate $h(\bar{n}, \bar{q}) = k_m \exp(-(V(\bar{n} = 0.5, \bar{q}) - V(\bar{n} = 1, \bar{q})))$, while the transition from $s = 1$ to $s = 0$ occurs with rate $f(\bar{n}, \bar{q}) = k_m \exp(-(V(\bar{n} = 0.5, \bar{q}) - V(\bar{n} = 0, \bar{q})))$.

APPENDIX C: DERIVING AN IMAGINARY-TIME SCHRÖDINGER EQUATION

In Sec. II C we rewrote the master equation as an imaginary time Schrödinger equation [Eq. (6)], where the stochastic Hamiltonian is given by Eq. (7). Since we model the contacts as a birth-death process, we use the following Poisson *ansatz* [15,20,26]:

$$|\Psi\rangle = \begin{pmatrix} c_1 \exp(\bar{q}_1(a^\dagger - 1))|\mathbf{0}\rangle \\ c_0 \exp(\bar{q}_0(a^\dagger - 1))|\mathbf{0}\rangle \end{pmatrix}, \quad (\text{C1})$$

$$\langle \Phi | = (\langle \mathbf{0} | e^{\alpha} \exp(\alpha_1 + \lambda_1 a) \quad \langle \mathbf{0} | e^{\alpha} \exp(\alpha_0 + \lambda_0 a)). \quad (\text{C2})$$

Furthermore, we impose $\langle \Phi(\alpha_L = 0) | \Psi(\alpha_R) \rangle = 1$. Plugging (C2) and (C1) into (8), we obtain the following set of variational equations given in Eq. (9).

APPENDIX D: DETAILS OF GILLESPIE STOCHASTIC SIMULATIONS

Stochastic simulations were carried out for the reaction network using an implementation of the Gillespie stochastic simulation algorithm [98] in Python using standard libraries. We set the parameters as follows: $c_n = 1.0 \tau^{-1}$, $c_r/c_n = 100.0$. We simulate a system of size $N = 40$ sites, and $M = 741$ mutable, nonbackbone contacts.

We ran simulations of length $3 \times 10^5 \tau$ using specified k_c/c_n , ϵ , λ values, approximately corresponding to $\sim 10^8 - 10^{10}$ Gillespie moves. We discarded the first half of each trajectory to remove the influence of initial conditions on the simulation results. Steady-state probability distributions and contact maps were obtained by averaging over the remaining half of each simulated trajectory.

To better understand the origin of the asymmetry in the epigenetic landscape presented in Fig. 2 of the main text, we computed the steady-state lifetime as follows. We identified the steady states using the fraction of modified nucleosomes as $\bar{n} \in (0.8, 1.0]$ and $\bar{n} \in [0.0, 0.2)$. To compute the average lifetimes of each, we subdivided the second half of each of the simulated trajectories into ~ 10 subtrajectories, each of length $10^4 \tau$; this allows one to observe at least $\sim 10^2$ transitions

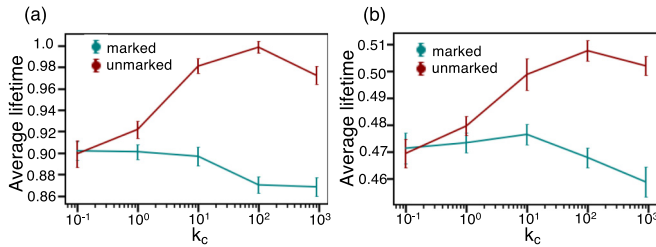


FIG. 12. Steady-state lifetime estimation is robust with respect to the state definition. Qualitatively similar trends to Fig. 3(c) of the main text are observed for marked (unmarked) states defined as (a) $(n) \in (0.9, 1.0]$ ($(n) \in [0.0, 0.1)$) and (b) $(n) \in (0.7, 1.0]$ ($(n) \in [0.0, 0.3)$).

between marked and unmarked states in each subtrajectory. A successful transition from the unmarked to marked state

was defined as the event wherein a system starting in the unmarked state arrives in the set defining the marked state (and vice versa). The lifetime of the unmarked (marked) state was defined to be the time between a transition to the unmarked (marked) state and transition to the marked (unmarked) state. The average lifetime was then obtained by computing the average time spent in each state in each subtrajectory, and the error bars in Fig. 3(c) reflect the standard error of the mean across the ten subtrajectories. A similar procedure was carried out to prepare Figs. 4(c), 5(c), 6(d), and 7(a)–7(c). We also tested the sensitivity of the results to the definition of marked (and unmarked) states used. We performed similar analysis by defining a marked (unmarked) state to be $\bar{n} \in (0.9, 1.0]$ ($\bar{n} \in [0.0, 0.1)$) and $\bar{n} \in (0.7, 1.0]$ ($\bar{n} \in [0.0, 0.3)$). Figure 12 demonstrates qualitatively similar trends for the average lifetimes with varying k_c using these thresholds to the ones seen in Fig. 3(c) of the main text.

- [1] A. Klosin and A. A. Hyman, A liquid reservoir for silent chromatin, *Nature (London)* **547**, 168 (2017).
- [2] X. Lin, Y. Qi, A. P. Latham, and B. Zhang, Multiscale modeling of genome organization with maximum entropy optimization, *J. Chem. Phys.* **155**, 010901 (2021).
- [3] T. Kouzarides, Chromatin modifications and their function, *Cell* **128**, 693 (2007).
- [4] A. D. Goldberg, C. D. Allis, and E. Bernstein, Epigenetics: A landscape takes shape, *Cell* **128**, 635 (2007).
- [5] B. Xhemalce, M. A. Dawson, and A. J. Bannister, Histone modifications, in *Reviews in Cell Biology and Molecular Medicine*, edited by R. A. Meyers (John Wiley & Sons, Ltd, 2011).
- [6] A. J. Bannister and T. Kouzarides, Regulation of chromatin by histone modifications, *Cell Res.* **21**, 381 (2011).
- [7] S. Mujtaba, L. Zeng, and M.-M. Zhou, Structure and acetyl-lysine recognition of the bromodomain, *Oncogene* **26**, 5521 (2007).
- [8] A. H. Hassan, P. Prochasson, K. E. Neely, S. C. Galasinski, M. Chandy, M. J. Carrozza, and J. L. Workman, Function and selectivity of bromodomains in anchoring chromatin-modifying complexes to promoter nucleosomes, *Cell* **111**, 369 (2002).
- [9] W. J. Xie and B. Zhang, Learning the formation mechanism of domain-level chromatin states with epigenomics data, *Biophys. J.* **116**, 2047 (2019).
- [10] R. Lister, M. Pelizzola, R. H. Dowen, R. D. Hawkins, G. Hon, J. Tonti-Filippini, J. R. Nery, L. Lee, Z. Ye, Q.-M. Ngo, L. Edsall, J. Antosiewicz-Bourget, R. Stewart, V. Ruotti, A. H. Millar, J. A. Thomson, B. Ren, and J. R. Ecker, Human DNA methylomes at base resolution show widespread epigenomic differences, *Nature (London)* **462**, 315 (2009).
- [11] R. Lu, F. Markowetz, R. D. Unwin, J. T. Leek, E. M. Airoidi, B. D. MacArthur, A. Lachmann, R. Rozov, A. Ma'ayan, L. A. Boyer, O. G. Troyanskaya, A. D. Whetton, and I. R. Lemischka, Systems-level dynamic analyses of fate change in murine embryonic stem cells, *Nature (London)* **462**, 358 (2009).
- [12] R. Margueron and D. Reinberg, Chromatin structure and the inheritance of epigenetic information, *Nat. Rev. Genet.* **11**, 285 (2010).
- [13] D. Moazed, Mechanisms for the inheritance of chromatin states, *Cell* **146**, 510 (2011).
- [14] R. Krishnakumar and W. L. Kraus, PARP-1 regulates chromatin structure and transcription through a KDM5B-dependent pathway, *Mol. Cell* **39**, 736 (2010).
- [15] M. Sasai and P. G. Wolynes, Stochastic gene expression as a many-body problem, *Proc. Natl. Acad. Sci. USA* **100**, 2374 (2003).
- [16] S. S. Ashwin and M. Sasai, Effects of collective histone state dynamics on epigenetic landscape and kinetics of cell reprogramming, *Sci. Rep.* **5**, 16746 (2015).
- [17] K. Zhang, M. Sasai, and J. Wang, Eddy current and coupled landscapes for nonadiabatic and nonequilibrium complex system dynamics, *Proc. Natl. Acad. Sci. USA* **110**, 14930 (2013).
- [18] B. Zhang and P. G. Wolynes, Stem cell differentiation as a many-body problem, *Proc. Natl. Acad. Sci. USA* **111**, 10185 (2014).
- [19] B. Bhattacharyya, J. Wang, and M. Sasai, Stochastic epigenetic dynamics of gene switching, *Phys. Rev. E* **102**, 042408 (2020).
- [20] A. Sood and B. Zhang, Quantifying the stability of coupled genetic and epigenetic switches with variational methods, *Frontiers in Genetics* **11**, 636724 (2021).
- [21] T. Parsons and B. Zhang, Critical role of histone tail entropy in nucleosome unwinding, *J. Chem. Phys.* **150**, 185103 (2019).
- [22] R. Cortini, M. Barbi, B. R. Care, C. Lavelle, A. Lesne, J. Mozziconacci, and J.-M. Victor, The physics of epigenetics, *Rev. Mod. Phys.* **88**, 025002 (2016).
- [23] C. Alabert, C. Loos, M. Voelker-Albert, S. Graziano, I. Forné, N. Reveron-Gomez, L. Schuh, J. Hasenauer, C. Marr, A. Imhof, and A. Groth, Domain model explains propagation dynamics and stability of H3K27 and H3K36 methylation landscapes, *Cell Rep.* **30**, 1223 (2020).
- [24] M. A. Micheelsen, N. Mitarai, K. Sneppen, and I. B. Dodd, Theory for the stability and regulation of epigenetic landscapes, *Phys. Biol.* **7**, 026010 (2010).

- [25] I. B. Dodd, M. A. Micheelsen, K. Sneppen, and G. Thon, Theoretical analysis of epigenetic cell memory by nucleosome modification, *Cell* **129**, 813 (2007).
- [26] A. Sood and B. Zhang, Quantifying epigenetic stability with minimum action paths, *Phys. Rev. E* **101**, 062409 (2020).
- [27] K. Sneppen and N. Mitarai, Multistability with a metastable mixed state, *Phys. Rev. Lett.* **109**, 100602 (2012).
- [28] D. Jost, Bifurcation in epigenetics: Implications in development, proliferation, and diseases, *Phys. Rev. E* **89**, 010701(R) (2014).
- [29] M. Sedighi and A. M. Sengupta, Epigenetic chromatin silencing: bistability and front propagation, *Phys. Biol.* **4**, 246 (2007).
- [30] A. Dayarian and A. M. Sengupta, Titration and hysteresis in epigenetic chromatin silencing, *Phys. Biol.* **10**, 036005 (2013).
- [31] W. Zhao, L. Qiao, S. Yan, Q. Nie, and L. Zhang, Mathematical modeling of histone modifications reveals the formation mechanism and function of bivalent chromatin, *iScience* **24**, 102732 (2021).
- [32] K. Newar, A. Z. Abdulla, H. Salari, E. Fanchon, and D. Jost, Dynamical modeling of the H3K27 epigenetic landscape in mouse embryonic stem cells, *PLoS Comput. Biol.* **18**, e1010450 (2022).
- [33] A. Z. Abdulla, C. Vaillant, and D. Jost, Painters in chromatin: a unified quantitative framework to systematically characterize epigenome regulation and memory, *Nucleic Acids Res.* **50**, 9083 (2022).
- [34] S. I. S. Grewal and D. Moazed, Heterochromatin and epigenetic control of gene expression, *Science* **301**, 798 (2003).
- [35] R. H. Jacobson, A. G. Ladurner, D. S. King, and R. Tjian, Structure and function of a human TAFII250 double bromodomain module, *Science* **288**, 1422 (2000).
- [36] D. J. Owen, P. Ornaghi, J.-C. Yang, N. Lowe, P. R. Evans, P. Ballario, D. Neuhaus, P. Filetici, and A. A. Travers, The structural basis for the recognition of acetylated histone H4 by the bromodomain of histone acetyltransferase Gcn5p, *The EMBO Journal* **19**, 6141 (2000).
- [37] G. Schotta, A. Ebert, V. Krauss, A. Fischer, J. Hoffmann, S. Rea, T. Jenuwein, R. Dorn, and G. Reuter, Central role of *Drosophila* SU(VAR)3-9 in histone H3-K9 methylation and heterochromatic gene silencing, *EMBO J.* **21**, 1121 (2002).
- [38] I. O. Torres and D. G. Fujimori, Functional coupling between writers, erasers and readers of histone and DNA methylation, *Curr. Opin. Struct. Biol.* **35**, 68 (2015).
- [39] R. Leicher, E. J. Ge, X. Lin, M. J. Reynolds, W. Xie, T. Walz, B. Zhang, T. W. Muir, and S. Liu, Single-molecule and in silico dissection of the interaction between Polycomb repressive complex 2 and chromatin, *Proc. Natl. Acad. Sci. USA* **117**, 30465 (2020).
- [40] F. Erdel and E. C. Greene, Generalized nucleation and looping model for epigenetic memory of histone modifications, *Proc. Natl. Acad. Sci. USA* **113**, E4180 (2016).
- [41] X. Lin, R. Leicher, S. Liu, and B. Zhang, Cooperative DNA looping by PRC2 complexes, *Nucleic Acids Res.* **49**, 6238 (2021).
- [42] L. Zhao, S. Wang, Z. Cao, W. Ouyang, Q. Zhang, L. Xie, R. Zheng, M. Guo, M. Ma, Z. Hu, W.-K. Sung, Q. Zhang, G. Li, and X. Li, Chromatin loops associated with active genes and heterochromatin shape rice genome architecture for transcriptional regulation, *Nat. Commun.* **10**, 3640 (2019).
- [43] X. Ding, X. Lin, and B. Zhang, Stability and folding pathways of tetra-nucleosome from six-dimensional free energy surface, *Nat. Commun.* **12**, 1091 (2021).
- [44] A. P. Latham and B. Zhang, Consistent force field captures homologue-resolved HP1 phase separation, *J. Chem. Theory Comput.* **17**, 3134 (2021).
- [45] A. G. Larson, D. Elnatan, M. M. Keenen, M. J. Trnka, J. B. Johnston, A. L. Burlingame, D. A. Agard, S. Redding, and G. J. Narlikar, Liquid droplet formation by HP1 α suggests a role for phase separation in heterochromatin, *Nature (London)* **547**, 236 (2017).
- [46] M. M. Keenen, D. Brown, L. D. Brennan, R. Renger, H. Khoo, C. R. Carlson, B. Huang, S. W. Grill, G. J. Narlikar, and S. Redding, HP1 proteins compact dna into mechanically and positionally stable phase separated domains, *eLife* **10**, e64563 (2021).
- [47] R. Tatavosian, S. Kent, K. Brown, T. Yao, H. N. Duc, T. N. Huynh, C. Y. Zhen, B. Ma, H. Wang, and X. Ren, Nuclear condensates of the Polycomb protein chromobox 2 (CBX2) assemble through phase separation, *J. Biol. Chem.* **294**, 1451 (2019).
- [48] N. J. Francis, R. E. Kingston, and C. L. Woodcock, Chromatin compaction by a polycomb group protein complex, *Science* **306**, 1574 (2004).
- [49] F. Nicol-Benoît, P. Le-Goff, Y. Le-Dréan, F. Demay, F. Pakdel, G. Flouriot, and D. Michel, Epigenetic memories: structural marks or active circuits? *Cell. Mol. Life Sci.* **69**, 2189 (2012).
- [50] T. Schlick, J. Hayes, and S. Grigoryev, Toward convergence of experimental studies and theoretical modeling of the chromatin fiber, *J. Biol. Chem.* **287**, 5183 (2012).
- [51] Y. Qi and B. Zhang, Predicting three-dimensional genome organization with chromatin states, *PLOS Comput. Biol.* **15**, e1007024 (2019).
- [52] K. Adachi and K. Kawaguchi, Chromatin state switching in a polymer model with mark-conformation coupling, *Phys. Rev. E* **100**, 060401(R) (2019).
- [53] S. H. Sandholtz, Q. MacPherson, and A. J. Spakowitz, Physical modeling of the heritability and maintenance of epigenetic modifications, *Proc. Natl. Acad. Sci. USA* **117**, 20423 (2020).
- [54] S. H. Sandholtz, D. Kannan, B. G. Beltran, and A. J. Spakowitz, Chromosome structural mechanics dictates the local spreading of epigenetic marks, *Biophys. J.* **119**, 1630 (2020).
- [55] J. F. Nickels, A. K. Edwards, S. J. Charlton, A. M. Mortensen, S. C. L. Hougaard, A. Trusina, K. Sneppen, and G. Thon, Establishment of heterochromatin in domain-size-dependent bursts, *Proc. Natl. Acad. Sci. USA* **118**, e2022887118 (2021).
- [56] M. J. Obersriebnig, E. M. H. Pallesen, K. Sneppen, A. Trusina, and G. Thon, Nucleation and spreading of a heterochromatic domain in fission yeast, *Nat. Commun.* **7**, 11518 (2016).
- [57] I. B. Dodd and K. Sneppen, Barriers and silencers: A theoretical toolkit for control and containment of nucleosome-based epigenetic states, *J. Mol. Biol.* **414**, 624 (2011).
- [58] M. Ancona, D. Michieletto, and D. Marenduzzo, Competition between local erasure and long-range spreading of a single biochemical mark leads to epigenetic bistability, *Phys. Rev. E* **101**, 042408 (2020).

- [59] D. Michieletto, M. Chiang, D. Coli, A. Papantonis, E. Orlandini, P. R. Cook, and D. Marenduzzo, Shaping epigenetic memory via genomic bookmarking, *Nucleic Acids Res.* **46**, 83 (2018).
- [60] D. Michieletto, E. Orlandini, and D. Marenduzzo, Polymer model with epigenetic recoloring reveals a pathway for the de novo establishment and 3D organization of chromatin domains, *Phys. Rev. X* **6**, 041047 (2016).
- [61] D. Michieletto, D. Coli, D. Marenduzzo, and E. Orlandini, Nonequilibrium theory of epigenomic microphase separation in the cell nucleus, *Phys. Rev. Lett.* **123**, 228101 (2019).
- [62] D. Jost, P. Carrivain, G. Cavalli, and C. Vaillant, Modeling epigenome folding: Formation and dynamics of topologically associated chromatin domains, *Nucleic Acids Res.* **42**, 9553 (2014).
- [63] D. Jost, C. Vaillant, and P. Meister, Coupling 1D modifications and 3D nuclear organization: data, models and function, *Curr. Opin. Cell Biol.* **44**, 20 (2017).
- [64] D. Jost and C. Vaillant, Epigenomics in 3d: importance of long-range spreading and specific interactions in epigenomic maintenance, *Nucleic Acids Res.* **46**, 2252 (2018).
- [65] J. D. Olarte-Plata, N. Haddad, C. Vaillant, and D. Jost, The folding landscape of the epigenome, *Phys. Biol.* **13**, 026001 (2016).
- [66] D. Coli, E. Orlandini, D. Michieletto, and D. Marenduzzo, Magnetic polymer models for epigenetics-driven chromosome folding, *Phys. Rev. E* **100**, 052410 (2019).
- [67] M. Katava, G. Shi, and D. Thirumalai, Chromatin dynamics controls epigenetic domain formation, *Biophys. J.* **121**, 2895 (2022).
- [68] S. Redding, Dynamic asymmetry and why chromatin defies simple physical definitions, *Curr. Opin. Cell Biol.* **70**, 116 (2021).
- [69] A. Zidovska, The self-stirred genome: large-scale chromatin dynamics, its biophysical origins and implications, *Curr. Opin. Genet. Dev.* **61**, 83 (2020), genome Architecture and Expression.
- [70] I. Eshghi, J. A. Eaton, and A. Zidovska, Interphase chromatin undergoes a local sol-gel transition upon cell differentiation, *Phys. Rev. Lett.* **126**, 228101 (2021).
- [71] J. Lerner, P. A. Gomez-Garcia, R. L. McCarthy, Z. Liu, M. Lakadamyali, and K. S. Zaret, Two-parameter mobility assessments discriminate diverse regulatory factor behaviors in chromatin, *Mol. Cell* **79**, 677 (2020).
- [72] S. S. Ashwin, T. Nozaki, K. Maeshima, and M. Sasai, Organization of fast and slow chromatin revealed by single-nucleosome dynamics, *Proc. Natl. Acad. Sci. USA* **116**, 19939 (2019).
- [73] S. Fujishiro and M. Sasai, Generation of dynamic three-dimensional genome structure through phase separation of chromatin, *Proc. Natl. Acad. Sci. USA* **119**, e2109838119 (2022).
- [74] H. Salari, M. Di Stefano, and D. Jost, Spatial organization of chromosomes leads to heterogeneous chromatin motion and drives the liquid- or gel-like dynamical behavior of chromatin, *Genome Res.* **32**, 28 (2022).
- [75] K. Kamat, Z. Lao, Y. Qi, Y. Wang, J. Ma, and B. Zhang, Compartmentalization with nuclear landmarks yields random, yet precise, genome organization, *Biophys. J.* **122**, 1376 (2023).
- [76] N. Khanna, Y. Zhang, J. S. Lucas, O. K. Dudko, and C. Murre, Chromosome dynamics near the sol-gel phase transition dictate the timing of remote genomic interactions, *Nat. Commun.* **10**, 2771 (2019).
- [77] C. P. Johnstone, N. B. Wang, S. A. Sevier, and K. E. Galloway, Understanding and engineering chromatin as a dynamical system across length and timescales, *Cell Syst.* **11**, 424 (2020).
- [78] B. Fierz and M. G. Poirier, Biophysics of chromatin dynamics, *Ann. Rev. Biophys.* **48**, 321 (2019).
- [79] H. Strickfaden, T. O. Tolsma, A. Sharma, D. A. Underhill, J. C. Hansen, and M. J. Hendzel, Condensed chromatin behaves like a solid on the mesoscale in vitro and in living cells, *Cell* **183**, 1772 (2020).
- [80] Y. Zhang, N. Liu, W. Lin, and C. Li, Quantifying the interplay between genetic and epigenetic regulations in stem cell development, *New J. Phys.* **21**, 103042 (2019).
- [81] N. Hathaway, O. Bell, C. Hodges, E. Miller, D. Neel, and G. Crabtree, Dynamics and memory of heterochromatin in living cells, *Cell* **149**, 1447 (2012).
- [82] A. N. Boettiger, B. Bintu, J. R. Moffitt, S. Wang, B. J. Believeau, G. Fudenberg, M. Imakaev, L. A. Mirny, C. T. Wu, and X. Zhuang, Super-resolution imaging reveals distinct chromatin folding for different epigenetic states, *Nature (London)* **529**, 418 (2016).
- [83] S. S. Rao, M. H. Huntley, N. C. Durand, E. K. Stamenova, I. D. Bochkov, J. T. Robinson, A. L. Sanborn, I. Machol, A. D. Omer, E. S. Lander, and E. L. Aiden, A 3D map of the human genome at kilobase resolution reveals principles of chromatin looping, *Cell* **159**, 1665 (2014).
- [84] J. D. Bryngelson and P. G. Wolynes, Spin glasses and the statistical mechanics of protein folding, *Proc. Natl. Acad. Sci. USA* **84**, 7524 (1987).
- [85] S. S. Plotkin and J. N. Onuchic, Structural and energetic heterogeneity in protein folding. I. Theory, *J. Chem. Phys.* **116**, 5263 (2002).
- [86] B. A. Shoemaker, J. Wang, and P. G. Wolynes, Exploring structures in protein folding funnels with free energy functionals: The transition state ensemble, *J. Mol. Biol.* **287**, 675 (1999).
- [87] B. A. Shoemaker and P. G. Wolynes, Exploring structures in protein folding funnels with free energy functionals: The denatured ensemble, *J. Mol. Biol.* **287**, 657 (1999).
- [88] H. Jacobson and W. H. Stockmayer, Intramolecular reaction in polycondensations. I. The theory of linear systems, *J. Chem. Phys.* **18**, 1600 (1950).
- [89] H. S. Chan and K. A. Dill, The effects of internal constraints on the configurations of chain molecules, *J. Chem. Phys.* **92**, 3118 (1990).
- [90] H. S. Chan and K. A. Dill, Intrachain loops in polymers: Effects of excluded volume, *J. Chem. Phys.* **90**, 492 (1989).
- [91] G. Schuette, X. Ding, and B. Zhang, Efficient Hi-C inversion facilitates chromatin folding mechanism discovery and structure prediction, *Biophys. J.* **122**, 3425 (2023).
- [92] T. Nozaki, R. Imai, M. Tanbo, R. Nagashima, S. Tamura, T. Tani, Y. Joti, M. Tomita, K. Hibino, M. T. Kanemaki, K. S. Wendt, Y. Okada, T. Nagai, and K. Maeshima, Dynamic organization of chromatin domains revealed by super-resolution live-cell imaging, *Mol. Cell* **67**, 282 (2017).

- [93] M. Ekeberg, C. Lövkvist, Y. Lan, M. Weigt, and E. Aurell, Improved contact prediction in proteins: Using pseudolikelihoods to infer Potts models, *Phys. Rev. E* **87**, 012707 (2013).
- [94] D. E. Makarov and H. Metiu, A model for the kinetics of protein folding: Kinetic Monte Carlo simulations and analytic results, *J. Chem. Phys.* **116**, 5205 (2002).
- [95] J. D. Bryngelson and P. G. Wolynes, Intermediates and barrier crossing in a random energy model (with applications to protein folding), *J. Phys. Chem.* **93**, 6902 (1989).
- [96] L. Kaustov, H. Ouyang, M. Amaya, A. Lemak, N. Nady, S. Duan, G. A. Wasney, Z. Li, M. Vedadi, M. Schapira, J. Min, and C. H. Arrowsmith, Recognition and specificity determinants of the human Cbx chromodomains, *J. Biol. Chem.* **286**, 521 (2011).
- [97] J. J. Funke, P. Ketterer, C. Lieleg, S. Schunter, P. Korber, H. Dietz, C. Lieleg, J. J. Funke, P. Ketterer, H. Dietz, and S. Schunter, Uncovering the forces between nucleosomes using DNA origami, *Sci. Adv.* **2**, e1600974 (2016).
- [98] D. T. Gillespie, Exact stochastic simulation of coupled chemical reactions, *J. Phys. Chem.* **81**, 2340 (1977).
- [99] H. Zhang, X.-J. Tian, A. Mukhopadhyay, K. S. Kim, and J. Xing, Statistical mechanics model for the dynamics of collective epigenetic histone modification, *Phys. Rev. Lett.* **112**, 068101 (2014).
- [100] M. I. Dykman, E. Mori, J. Ross, and P. M. Hunt, Large fluctuations and optimal paths in chemical kinetics, *J. Chem. Phys.* **100**, 5735 (1994).
- [101] P. Zhou and T. Li, Construction of the landscape for multi-stable systems: Potential landscape, quasi-potential, A-type integral and beyond, *J. Chem. Phys.* **144**, 094109 (2016).
- [102] J. Wang, K. Zhang, and E. Wang, Kinetic paths, time scale, and underlying landscapes: A path integral framework to study global natures of nonequilibrium systems and networks, *J. Chem. Phys.* **133**, 125103 (2010).
- [103] D. Liu, Optimal transition paths of stochastic chemical kinetic systems, *J. Chem. Phys.* **124**, 164104 (2006).
- [104] D. M. Roma, R. A. O'Flanagan, A. E. Ruckenstein, A. M. Sengupta, and R. Mukhopadhyay, Optimal path to epigenetic switching, *Phys. Rev. E* **71**, 011902 (2005).
- [105] J. M. Eeftens, M. Kapoor, D. Michieletto, and C. P. Brangwynne, Polycomb condensates can promote epigenetic marks but are not required for sustained chromatin compaction, *Nat. Commun.* **12**, 5888 (2021).
- [106] Our code is available at <https://github.com/ZhangGroup-MITChemistry/CodeDynPTChrXHist>.
- [107] S. Plimpton, Fast parallel algorithms for short-range molecular dynamics, *J. Comput. Phys.* **117**, 1 (1995).